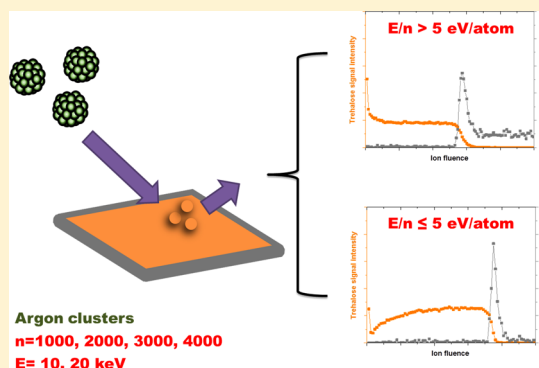


Molecular Depth Profiling with Argon Gas Cluster Ion Beams

Kan Shen,[†] Andreas Wucher,[‡] and Nicholas Winograd^{*,†}[†]Department of Chemistry, The Pennsylvania State University, University Park, Pennsylvania 16802, United States[‡]Department of Physics, University of Duisburg-Essen, 47048 Duisburg, Germany

S Supporting Information

ABSTRACT: Argon gas cluster ion beams (Ar-GCIBs) are remarkable new projectiles for secondary ion mass spectrometry (SIMS) depth profiling of organic materials. However, the optimal cluster size and kinetic energy to provide the best quality of depth profiles, in terms of high ionization efficiency of the target molecules, little chemical damage, and short experiment time, for organic materials is not fully understood. Hence, the effect of cluster size and kinetic energy on the quality of molecular depth profiling is investigated on a simple platform composed of trehalose thin films to acquire more fundamental information about the ion/solid interaction. The results suggest that the sputter yield (Y/n) of argon clusters is linearly dependent upon kinetic energy per atom (E/n). When $E/n > 5$ eV/atom, normal depth profiles are obtained with relatively high sputter yields. When $E/n \leq 5$ eV/atom, however, distorted depth profiles in the steady state region are observed, which exhibit a low sputter yield and variable ionization efficiency. As a consequence of these observations, it was concluded that high kinetic energy increases the useful molecular ion yield of trehalose and that Ar_n^+ clusters with a small E/n value minimize ion beam bombardment induced chemical damage. Hence optimal conditions for molecular depth profiling will be obtained using the highest kinetic energy with the largest clusters while maintaining a value of E/n near a threshold value of 5 eV/atom. In general, this study provides insight into selecting optimal Ar-GCIB characteristics for molecular depth profiling of organic materials.



INTRODUCTION

Secondary ion mass spectrometry (SIMS) has been used as an in-depth characterization method for inorganic materials, particularly semiconductors, for many years.^{1–3} To expand the scope of this technique into the investigation of organic samples, there has been a growing emphasis on the development of cluster ion sources, such as Au_3 ,^{4,5} Bi_3 ,⁶ SF_5 ,⁷ and C_{60} .⁴ These probes, particularly C_{60} , are more effective than the traditional atomic ion sources, because less chemical damage is accumulated during the interaction of the projectiles with the solid. Molecular depth profiling of a variety of organic materials is now possible,^{8–11} providing an important new characterization modality for SIMS. Recently, argon gas cluster ion beams (Ar-GCIBs)¹² have generated a great deal of excitement, because they appear to yield better depth resolution and produce less chemical damage than C_{60} ,^{13–16} broadening the scope of this technology even further.

There is flexibility associated with the implementation of GCIBs. For example, the nature of the chemical composition of these clusters can be varied, consisting of water clusters^{17,18} or Ar clusters doped with other species such as CO_2 ¹⁵ and CH_4 ,¹⁹ or other molecules such as N_2 ²⁰ and $\text{C}_2\text{H}_5\text{OH}$.^{21,22} The idea behind many of these experiments is to increase the ionization efficiency of the target molecules by providing a source of protons for making $[\text{M} + \text{H}]^+$ ions. Other dopants such as CO_2 appear to provide a stabilizing effect on the cluster, yielding better focusing properties for imaging.¹⁵

At a more basic level, however, it is also possible to vary the cluster size, mass, and kinetic energy over wide ranges. There have been attempts to predict how the sputtering yield and the ionization probability depend upon these parameters using both fundamental²³ and empirical^{24,25} approaches that have helped to begin to organize available data in a consistent fashion. In addition, there have been several Ar-GCIB studies that have focused on how the depth resolution obtained during molecular depth profiling of multilayer structures depends upon cluster size and kinetic energy.^{26,27} To achieve a molecular depth profile in the shortest time, with the best ionization efficiency and with the fewest sputter-induced artifacts, there surely exists a complex interplay between these parameters that has yet to be worked out.

Here, we examine depth profiles of 150 nm spin-cast thin films of trehalose deposited onto Si wafers. The profiles were obtained under various conditions using the Ar-GCIB projectile for sputtering and for analysis. We limited the study to pure Ar-GCIBs to avoid chemical effects associated with reactive species. Trehalose is chosen as a model substrate because it has been extensively used by us to determine appropriate conditions for C_{60} depth profiling and it has been successfully characterized with an erosion dynamics model to measure the thickness of the

Received: April 10, 2015

Revised: May 18, 2015

Published: June 8, 2015

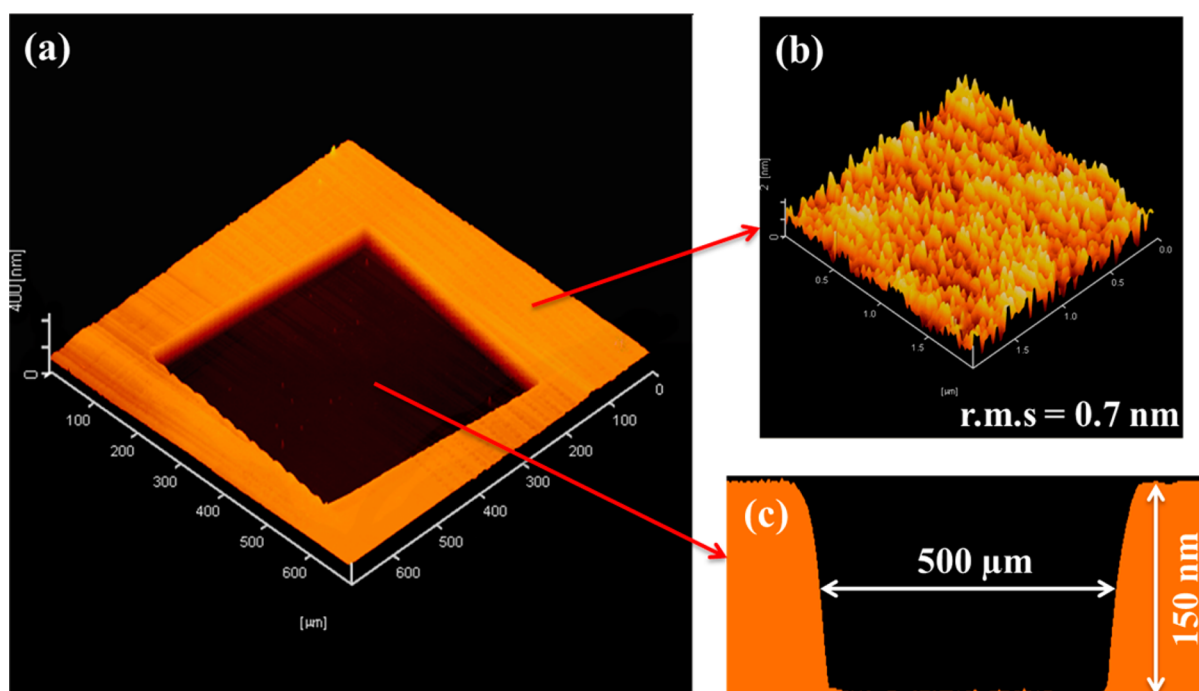


Figure 1. AFM images of a trehalose film bombarded by a 40 keV C_{60}^+ ion beam. Image a shows the bombarded region of the film in three dimensions. Image b shows that the unbombarded region of the film has a 0.7 nm rms roughness. Image c shows a line scan taken across the bombarded region of the film, which indicates that the film has a thickness of 150 nm.

altered layer at the surface, depth resolution, sputtering yield, and damage cross section.^{28–30} Following this methodology, we examine depth profiles obtained using kinetic energies of 10 and 20 keV with cluster sizes of Ar_{1000} , Ar_{2000} , Ar_{3000} , and Ar_{4000} . With this approach, it is possible to quantitatively determine how the important parameters affect the shape and the intensity of the depth profile. Perhaps most importantly, this study suggests that the best situation results from using the highest kinetic energy and the largest possible cluster with an E/n value slightly larger than 5 eV/atom. This finding is in agreement with recently published studies in the static SIMS regime, which state that high energy and larger clusters are beneficial for increasing the molecular ion yield of organic materials.^{15,18}

EXPERIMENTAL SECTION

Material and Sample Preparation. Presliced 5 mm × 5 mm Si wafers (Ted Pella Inc., Reading, CA, USA) were used as substrates for all films. The substrates were piranha etched (3:1 H_2SO_4/H_2O_2) for 20 min and rinsed with deionized water three times to remove contaminants from the substrates and make the substrate surface hydrophilic. (*Extreme caution must be exercised when using piranha etch. An explosion-proof hood should be used.*) Trehalose (Sigma-Aldrich Co., St. Louis, MO, USA) films were prepared by spin-casting 50 μL of a 0.5 M aqueous trehalose solution in 10 μL aliquots onto the cleaned Si wafers. Each aliquot was allowed to spin for 30 s at 5000 rpm before the subsequent aliquot was applied. A uniformly colored film with a glassy appearance is normally obtained. The freshly prepared films were immediately transferred to the ToF-SIMS instrument for measurement to minimize surface contamination.

Instrumentation. Sample analysis was performed using a J105 3D Chemical Imager (Ionoptika Ltd., Chandlers Ford, UK), the design of which has been described previously.³¹ The instrument is equipped with a 40 kV C_{60} primary ion beam and a 20 kV Ar-GCIB system. Unlike conventional ToF-SIMS

instruments that operate alternatively between data acquisition cycles in pulsed mode and erosion cycles in DC mode, this J105 instrument uses a continuous primary ion beam to generate a continuous stream of secondary ions. The secondary ions are collected in a buncher and then accelerated into a ToF analyzer. This design allows for continuous data collection and ensures that no sample information is lost. In this study, trehalose films were first investigated with a 40 keV C_{60}^+ ion beam. SIMS images of 64 × 64 pixels and corresponding mass spectra were collected from an area of 500 μm × 500 μm with an ion fluence of $\sim 1.3 \times 10^{12}$ ions/ cm^2 per image. Depth profiles and ion intensity measurement were collected from the central 13 × 13 pixels of each image, thus eliminating the crater edge effects. The gathered sputter yield and beam-induced chemical damage information were compared to earlier measurements³⁰ that were carried out on a traditional ToF-SIMS instrument. The design and characteristics of the 20 kV Ar-GCIB system have been described in detail elsewhere.¹³ In the Ar-GCIB experiments, the cluster size distribution can be checked by pulsing the ion beam and measuring the flight time of the primary ions between the pulser and the sample stage (see S1 in the Supporting Information). From the known flight distance and kinetic energy, the flight time spectrum can be used to determine the average cluster size of the beam and a Wien filter is used for selecting cluster ions of the desired size. In this study, we have Ar_{1000} , Ar_{2000} , Ar_{3000} , and Ar_{4000} cluster ions at kinetic energies of 10 and 20 keV, respectively. For each gas cluster, the primary ion beam current was measured using a Faraday cup, and the beams used were all adjusted to provide ~ 90 –120 pA beam currents. The experimental setup was the same as described above except that the ion fluence applied here was higher, $\sim 5.5 \times 10^{12}$ ions/ cm^2 per image. Note that in this study all of the depth profiling experiments were performed in negative ion mode at room temperature and no sign of sample charging was noticed.

Atomic Force Microscopy (AFM) Measurements. The trehalose film thickness was measured by an AFM (Nanopics 2100, KLA-Tencor, San Jose, CA, USA). This unique type of AFM offers a maximum scanning area of 0.8 mm × 0.8 mm in contact mode, allowing a convenient one-step measurement of the entire eroded crater. An AFM image of a trehalose film eroded by a 40 keV C₆₀⁺ ion source is illustrated in Figure 1. The AFM measurement indicates a 0.7 nm root-mean-square (rms) film roughness and a 150 nm film thickness. Note that the erosion rate of Si is significantly slower than that of trehalose. Therefore, the removed Si thickness should be negligible. This AFM was also employed to determine sputtering yields via the formation of a wedge-shaped crater.³²

RESULTS AND DISCUSSION

Negative Secondary Ion Depth Profiles of Trehalose Films Bombarded by C₆₀⁺. The negative secondary ion depth profile for a 150 nm trehalose film on Si bombarded by 40 keV C₆₀⁺ is shown in Figure 2a, where the trehalose molecular ion (M – H)[–] at *m/z* 341 and substrate signal at *m/z* 168 for Si₆[–] are plotted as a function of C₆₀⁺ ion fluence. A total ion fluence of ~1.05 × 10¹⁴ ions/cm² is used to etch through the film before reaching the Si substrate. The sputter yield volume of trehalose is calculated from the known fluence and film thickness and is

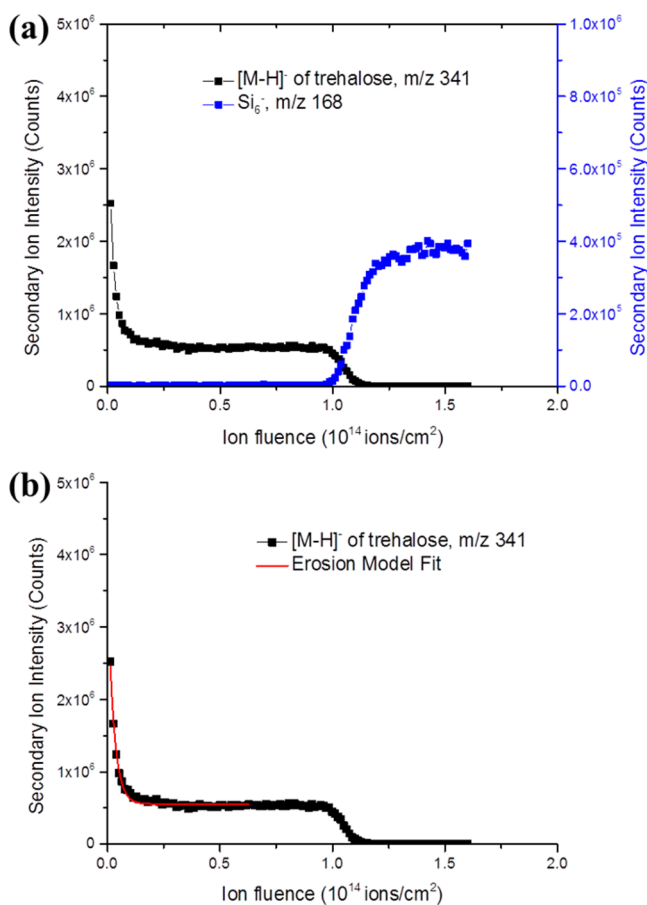


Figure 2. (a) Depth profile of a 150 nm trehalose film obtained with a 40 keV C₆₀⁺ ion beam. The secondary ion intensities of the trehalose molecular ion peak at *m/z* 341 [M – H][–] and substrate signal at *m/z* 168 for Si₆[–] are plotted as a function of C₆₀⁺ ion fluence. (b) Erosion model fit (red line) for the trehalose molecular ion signal in the depth profile of a 150 nm trehalose film bombarded by 40 keV C₆₀⁺.

presented in units of sputtered material volume per projectile ion. In this case, one C₆₀⁺ primary ion removes 143 nm³ of material, a value consistent with earlier measurements.³⁰ In addition, an erosion model developed by Cheng et al.²⁹ is used to fit the trehalose molecular ion decay profile to quantify the ion beam bombardment induced chemical damage, as shown in Figure 2b. According to the model, the dependence of the secondary ion signal *S* on ion fluence *f* is governed by

$$S(f) = S_{ss} + (S_0 - S_{ss}) \exp\left[-\left(\frac{Y}{d} + \sigma_D\right)f\right] \quad (1)$$

where *S*₀ is the signal intensity at zero fluence, *S*_{ss} is the signal intensity at steady state, *Y* is the sputter yield volume, *d* is the altered layer thickness, σ_D is the damage cross section, and *f* is the primary ion fluence. The value of *S*_{ss} is also related to *Y* and primary ion beam induced damage as

$$S_{ss} = S_0 \frac{Y}{Y + d\sigma_D} \quad (2)$$

The two variables associated with chemical damage, *d* and σ_D , can then be extracted from eqs 1 and 2. For our sample, *d* and σ_D are calculated to be ~25 and ~30 nm², respectively. These values are slightly higher than our earlier results,³⁰ which is probably associated with the intrinsic water content of the deposited films, as explained by Lu et al.³³ Trehalose films with less water content have a larger ratio value between the initial and steady state signal, indicating an enhanced damage cross section during the ion bombardment, which is the case for the trehalose films investigated in this study. Note that in the previous work, trehalose thin films were all analyzed in positive ion mode, where the trehalose molecular ion peak [M + H]⁺ at *m/z* 343 is of low intensity and the two most abundant trehalose molecule related peaks are quasi-molecular ions [M – OH]⁺ at *m/z* 325 and the sodium adduct [M + Na]⁺ at *m/z* 365. There is less interference of trehalose molecular ion information in negative ion mode, where the only predominant peak of trehalose molecule is [M – H][–] at *m/z* 341.

Negative Secondary Ion Depth Profiles of Trehalose Films Bombarded by Ar-GCIBs. Eight negative secondary ion depth profiles of the trehalose films obtained using different kinetic energies (*E*) and Ar cluster sizes (*n*) are presented in Figure 3. Depth profiles shown in Figure 3, panels a–c and e, exhibit a shape similar to the one obtained with C₆₀⁺; namely, the trehalose molecular ion falls quickly into a steady state value. The depth profiles shown in Figure 3, panels d and f–h, however, are distinctly different. In these cases, the trehalose signal initially decreases and then slowly increases to reach a steady state. Note that these unusual depth profiles appear only when *E/n* ≤ 5 eV/atom. Speculation about the reasons behind this behavior is discussed below.

Values of the trehalose sputter yield volume at different kinetic energies and Ar cluster sizes are summarized in Table 1. These results clearly indicate that the sputter yield volume is affected by a combination of kinetic energy and Ar cluster size. Briefly, as shown in Figure 4, the trehalose sputter yield volume decreases with increasing Ar cluster sizes at a given kinetic energy. Moreover, for the same cluster size, the sputter yield volume increases with increasing kinetic energy. Seah²⁴ has introduced a universal equation for Ar gas cluster sputtering yields to organize the experimental data and to allow rational comparisons to be made. The universal equation that describes the relationship

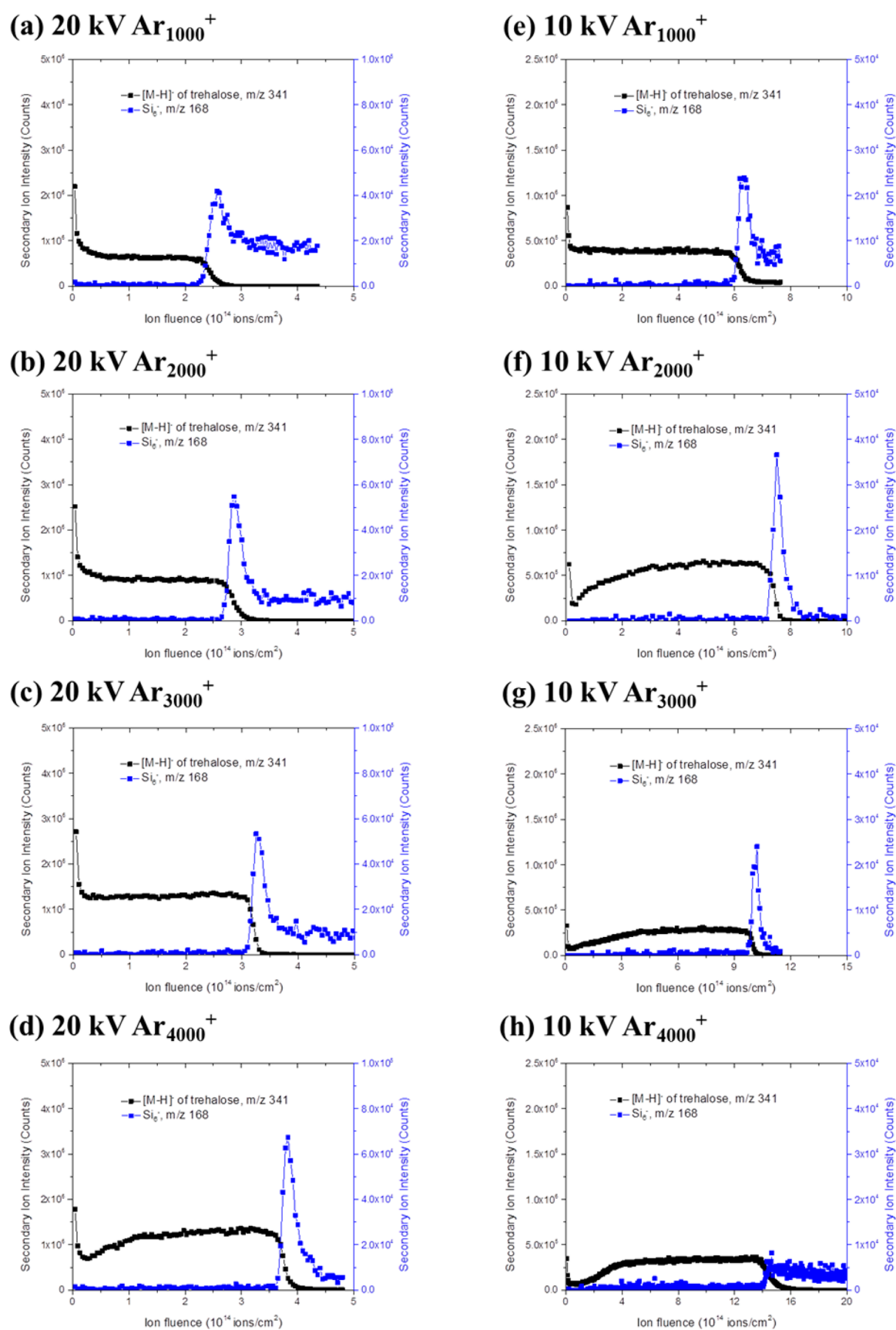


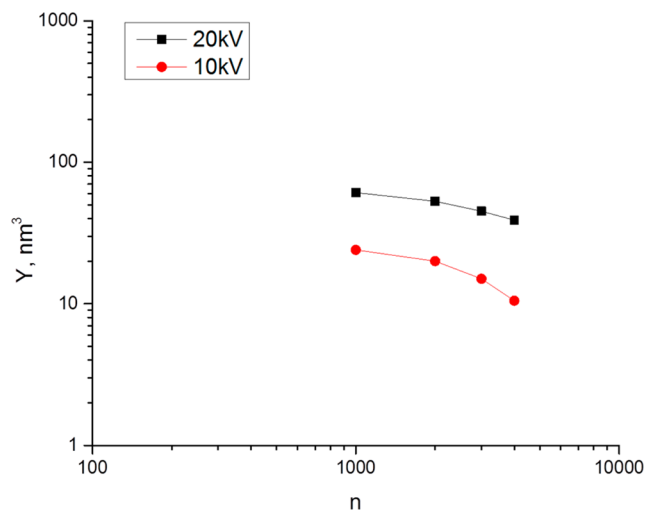
Figure 3. Depth profiles of the 150 nm trehalose films obtained with 10 kV and 20 kV Ar_n^+ ion beams.

between sputter yield volume per atom (Y/n) and the kinetic energy per atom (E/n) is defined as

$$Y/n = B(E/An)^q / [1 + (E/An)^{q-1}] \quad (3)$$

Table 1. Measured Trehalose Sputter Yield Volume for Different Kinetic Energies and Cluster Sizes of Ar-GCIBs

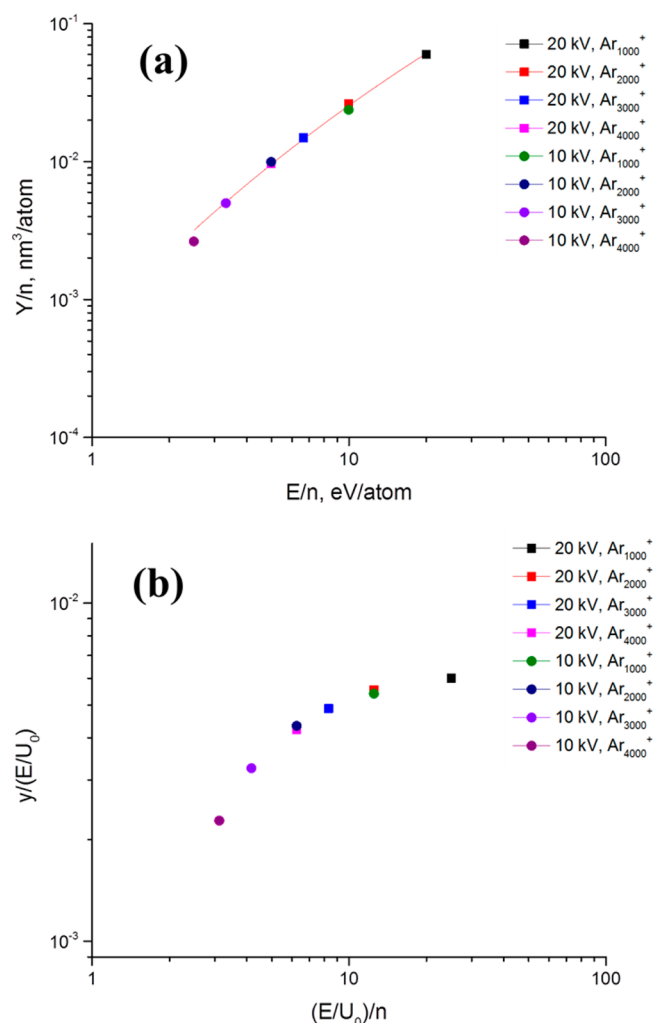
kinetic energy (kV)	sputter yield volume (nm ³)			
	Ar ₁₀₀₀ ⁺	Ar ₂₀₀₀ ⁺	Ar ₃₀₀₀ ⁺	Ar ₃₀₀₀ ⁺
20	61	53	45	39
10	24	20	15	10

**Figure 4.** Dependence of sputter yield volume (Y) on cluster size (n) for Ar_n^+ cluster bombardment of trehalose films.

where the parameters B , A , and q can be determined by fitting eq 3 to the experimental data. Our results show that Y/n exhibits a nearly linear dependence on E/n and the parameters B , A , and q have values of 0.018 nm³, 4.8 eV, and 2.0, respectively. These values are close to the ones reported for other organic materials.^{24,34}

Using a more fundamental approach, Paruch et al.²³ have recently suggested taking cohesive energy (U_0) of the analyte into consideration. Therefore, our data were replotted as $y/(E/U_0)$ versus $(E/U_0)/n$, as shown in Figure 5b. Note that y is the sputter yield in units of sputtered material molecules per projectile ion and U_0 is defined as the energy needed to free a molecule from the substrate. For trehalose, it is mainly the intermolecular hydrogen bond attractions that hold the substance together, and its cohesive energy is estimated to be ~ 0.8 eV for a trehalose molecule. The estimation is based on the assumption that the cohesive energy is equal to the heat of sublimation.^{35,36} The plot shows that in the low $(E/U_0)/n$ portion, the sputter yield is low and increases with increasing energy, whereas when it passes the threshold value ($(E/U_0)/n = S/U_0$), the sputter yield remains almost constant. The low sputter yield in the low $(E/U_0)/n$ portion is probably associated with the unusual depth profiles shown in Figure 3d,f–h. We will come back to this issue below.

The next step is to gain a better understanding of the molecular sputtering process of the trehalose films under Ar_n^+ cluster bombardment, specifically regarding the creation of chemical damage. The erosion model mentioned earlier can be successfully applied to those normal trehalose molecular ion depth profiles shown in Figure 3a–c,e. The calculated d and σ_D values are ~ 5 and 17 nm², 17 and 17 nm², 13 and 19 nm², and 10 and 23 nm² for 10 kV Ar₁₀₀₀⁺, 20 kV Ar₁₀₀₀⁺, 20 kV Ar₂₀₀₀⁺, and 20 kV Ar₃₀₀₀⁺, respectively. It appears that for the same cluster (Ar_{1000}^+), higher kinetic energy yields a higher d value, whereas

**Figure 5.** (a) Dependence of Y/n on E/n for Ar_n^+ cluster bombardment of trehalose films. The red line represents a fit to the universal equation (eq 3) for argon gas cluster sputtering yields proposed by Seah.²⁴ (b) Dependence of $y/(E/U_0)$ on $(E/U_0)/n$ for Ar_n^+ cluster bombardment of trehalose films.

σ_D remains nearly constant. Moreover, the results show that the d value is decreasing with increasing cluster size at 20 kV ($\text{Ar}_{1000}^+ < \text{Ar}_{2000}^+ < \text{Ar}_{3000}^+$), whereas σ_D is increasing with increasing cluster size. It seems that σ_D is related to the actual size of the cluster. Therefore, a larger cluster will have a higher σ_D value. The d value is mainly associated with E/n . At the same kinetic energy, a larger cluster has a lower value of E/n , so the energy is deposited closer to the surface, which results in a smaller d value.

The intensity of the first data point of each depth profile acquired with Ar_n^+ is shown in Figure 6 as a function of E/n , and one finds that Ar_n^+ with a smaller E/n value has a smaller fragment to molecular ion ratio, which indicates less damage. This finding can be further confirmed from the trehalose molecular ion depth profiles shown in Figure 3, where the span between trehalose molecular ion intensity at the first data point and the steady state becomes narrower as the E/n value decreases. Note that the signal level of the first acquired data point on the freshly prepared trehalose film is quite reproducible and no significant fluctuation is observed. In principle, the unusual shape of the profiles shown in Figure 3d,f–h can also be interpreted in terms of the erosion dynamics model, if the assumption of a constant total sputter yield is dropped.³⁷ If the

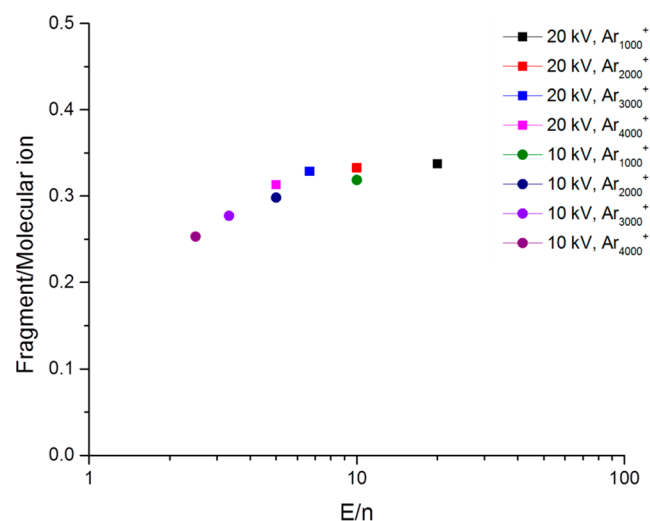


Figure 6. Dependence of the ratio of the intensity of the trehalose fragment at m/z 179 to the trehalose molecular ion at m/z 341 from the first data point of each depth profile as a function of E/n .

yield variation is slow, the system will follow eq 1 into a quasi-steady-state regime, where the molecular ion signal follows a gradual change of Y via eq 2. The observed signal rise would then correspond to an increasing sputter yield, which leads to a faster removal of the fragmentation debris produced by a projectile impact. As a consequence, the accumulated damage should be reduced and one should observe a decreasing signal of fragments as compared to the molecular ion. The ratio of the intensity of the trehalose fragment at m/z 179 to the trehalose molecular ion at m/z 341 as a function of primary ion fluence is displayed in Figure 7. It is evident that the ratio increases with increasing fluence, indicating the buildup of more damage while the molecular ion signal increases. To examine the role of possible

sputter yield variations further, a wedge crater was eroded as shown in Figure 8. Briefly, the wedge crater was created by

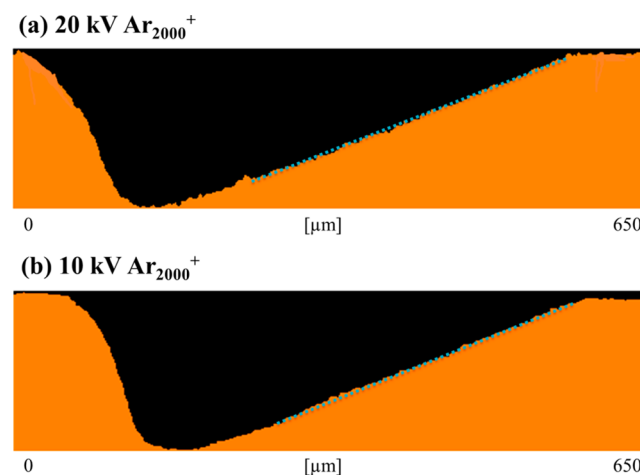


Figure 8. AFM image of the wedge crater eroded into a 150 nm trehalose film by (a) a 20 kV Ar_{2000}^+ ion beam and (b) a 10 kV Ar_{2000}^+ ion beam. Note the slope of the bevel remains as a straight line before the crater reaches the Si substrate.

repeating the raster as many times as there are pixels in one line or lines in one raster frame. In each of these raster frames, one more line was skipped. In our case, the beam was scanned across a $500 \mu\text{m} \times 500 \mu\text{m}$ area using a 64×64 pixel raster. The raster was repeated 64 times, scanning 64 lines in the first frame, 63 lines in the second frame, etc., until the last scan was only over a single line. One set of these wedge frames therefore consists of 64 rasters. The dwell time on each pixel was set to about 20 μs , which is the minimum dwell time that ensures stable beam position on a pixel. The number of wedge frame sets during a

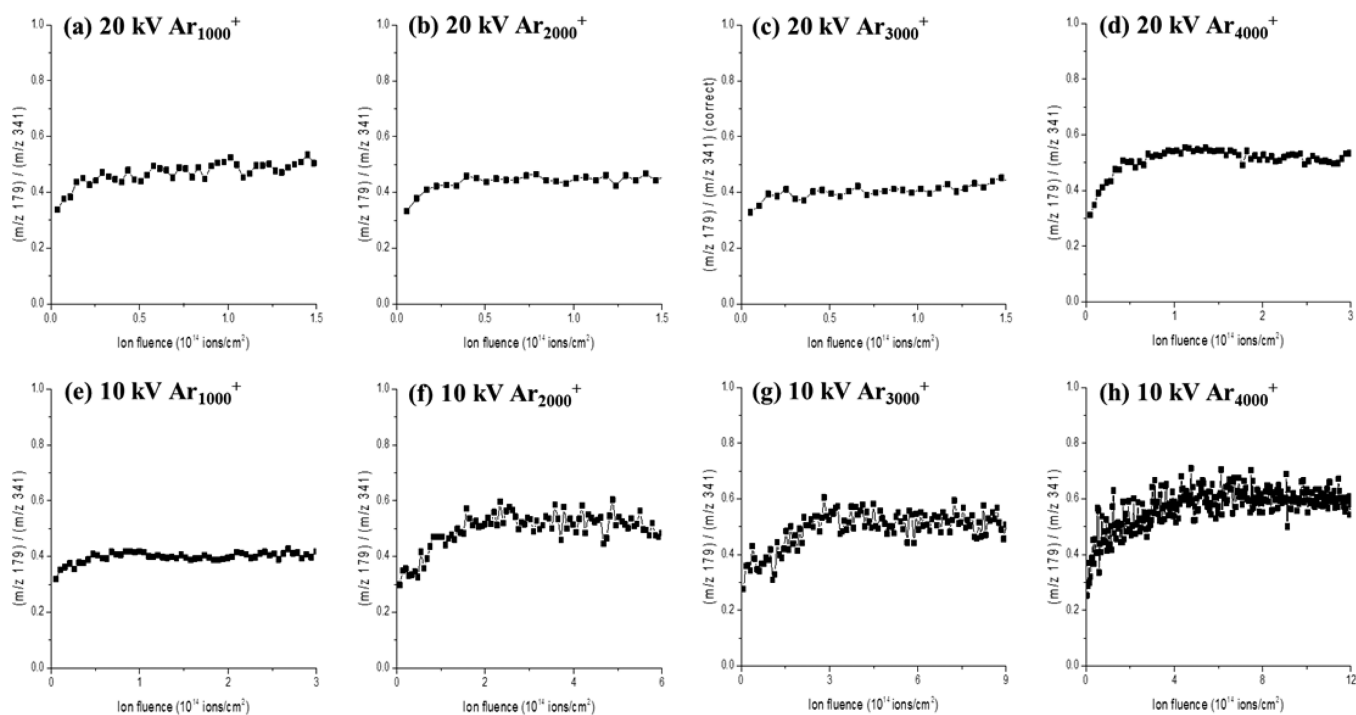


Figure 7. Ratio profiles of the intensity of the trehalose fragment (m/z 179) to the intensity of trehalose molecular ion (m/z 341) as a function of ion fluence under different Ar_n^+ bombarding conditions.

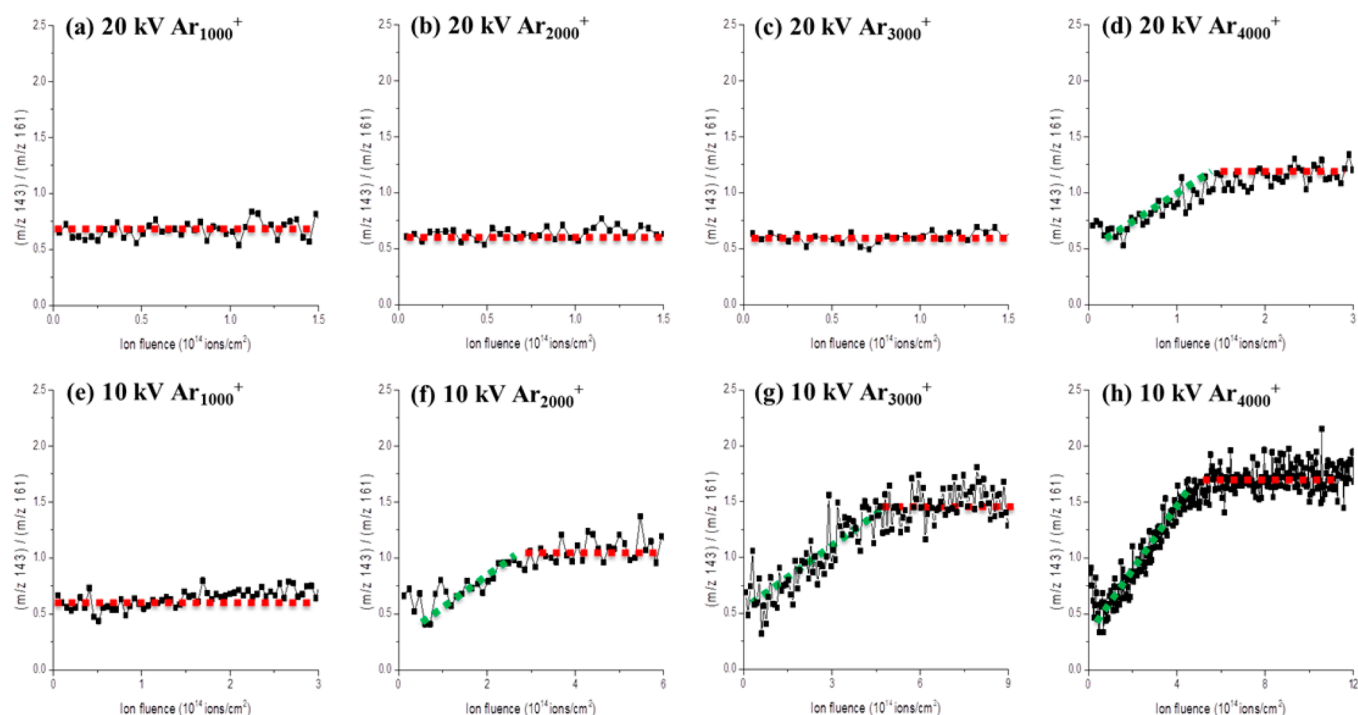


Figure 9. Ratio profiles of the intensity of two characteristic trehalose fragments (m/z 143 to m/z 161) as a function of ion fluence under different Ar_n^+ bombarding conditions.

sputter erosion step was calculated such that the set total sputtering time in an erosion cycle was reached. As outlined in detail elsewhere, a fluence-dependent sputter yield variation manifests itself as a curved crater bottom in such an experiment.³⁸ Because all craters observed in Figure 8 exhibit a straight line profile, the unusually shaped depth profiles are not caused by a variation in sputter yield.

Now, the remaining question is what factor leads to the two different shapes of trehalose molecular ion depth profiles shown in Figure 3. If sputter yield changes are excluded, possible explanations for the observed increase of the molecular ion signal are that there is an increasing survival probability against fragmentation or that there is an enhanced ionization of the sputtered molecules. To examine this further, the ratio of the intensity of two characteristic trehalose fragments (m/z 143 to m/z 161) is plotted as a function of ion fluence for each Ar_n^+ bombarding condition, as presented in Figure 9. For those normal trehalose molecular ion depth profiles shown in Figure 3a–c,e, this ratio remains virtually constant, see Figure 9a–c,e, which confirms that a true steady state is reached under these conditions. Note that for all of these conditions, $E/n > 5$ eV/atom. However, for the unusual depth profiles shown in Figure 3d,f–h, the ratio between the two fragments increases throughout the same fluence interval where the molecular ion signal increases, until it finally reaches a steady state, as shown in Figure 9d,f–h. In connection with Figure 7, this finding indicates that the observed increase of the molecular ion signal is accompanied by increasing fragmentation as well. Hence, this signal increase must be attributed to an increasing ionization probability of the emitted molecules. Note that the mass difference (Δm) between the two fragments is 18, which indicates that there could be a water content change during the depth profiling. The extra water can cause trehalose ionization probability to increase during the experiments.³³

Finally, it is possible to acquire information about the useful yield of trehalose under different Ar_n^+ bombarding conditions. Here, the useful yield is defined as the ratio of the number of detected molecular ions to the number of the sputtered molecule equivalents, and its value is estimated via

$$\text{useful yield} = S_1/[f \times A \times y] \quad (4)$$

where S_1 is the molecular ion signal intensity at the first data point, f is the primary ion fluence used to take the spectra, A is the data analysis area, and y is the sputter yield in units of sputtered molecule equivalents per projectile ion. Note that the amount of signal transmission loss in the mass spectrometer is not considered here. As shown in Figure 10, the useful molecular

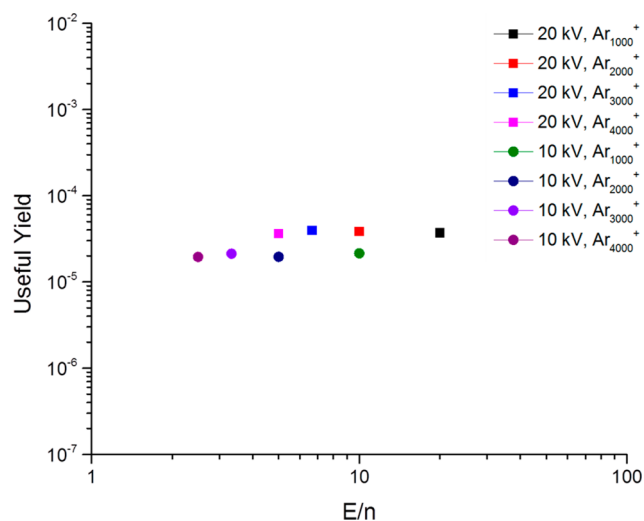


Figure 10. Dependence of useful molecular ion yield of trehalose on E/n for Ar_n^+ cluster bombardment of trehalose films.

ion yield of trehalose increases with increasing kinetic energy but remains almost the same with increasing Ar cluster sizes at a given kinetic energy, indicating that the useful yield is dependent only upon kinetic energy.

CONCLUSION

The effect of projectile size and kinetic energy of Ar-GCIBs on the molecular depth profiling of trehalose thin films has been investigated with the purpose of finding the optimal cluster size and cluster energy to improve the quality of depth profiles for organic materials. Our results suggest that when $E/n > 5$ eV/atom, normal depth profiles could be obtained with relatively high sputter yield, whereas when $E/n \leq 5$ eV/atom, unusual depth profiles, which show ionization efficiency variation, are acquired with low sputter yield. However, this observation does not imply that E/n values should be as high as possible. In fact, the E/n value should be kept above but close to the threshold value (5 eV/atom in our case) because ion beam bombardment induced chemical damage is limited.

Although this study has focused upon using trehalose as a model system, we believe the conclusions can be generalized for many other organic materials. In preliminary studies, we have found similar behavior for other organic thin films including sucrose, dipalmitoylphosphatidylcholine (DPPC), and Gly-Gly-Tyr-Arg (GGYR) (see S2 in the Supporting Information). It will be of interest to determine how much the threshold value for creating depth profiles without artifacts changes with molecule type. In general, however, our study shows that high kinetic energy increases the useful molecular ion yield of trehalose. Hence, a combination of high kinetic energy and large cluster size will ultimately optimize molecular depth profiling experiments with SIMS.

ASSOCIATED CONTENT

Supporting Information

Depth profiles of sucrose, DPPC, and GGYR thin films obtained with a 20 kV Ar₄₀₀₀⁺ ion beam. The Supporting Information is available free of charge on the ACS Publications website at DOI: 10.1021/acs.jpcc.5b03482.

AUTHOR INFORMATION

Corresponding Author

*(N.W.) E-mail: nxw@psu.edu. Fax: (814) 863-0618.

Notes

The authors declare no competing financial interest.

ACKNOWLEDGMENTS

We appreciate the contributions of Dr. Hua Tian in optimizing the instrumentation in these studies. This study was financially supported by National Institutes of Health Grant 9R01 GM113746-20A1. In addition, infrastructure support from the National Science Foundation under Grant CHE-0908226 and by the Division of Chemical Sciences at the Department of Energy (Grant DE-FG02-06ER15803) is acknowledged.

REFERENCES

- (1) Liebl, H. Secondary-Ion Mass Spectrometry and Its Use in Depth Profiling. *J. Vac. Sci. Technol.* **1975**, *12*, 385–391.
- (2) Magee, C. W.; Harrington, W. L.; Botnick, E. M. On the Use of CsX⁺ Cluster Ions for Major Element Depth Profiling in Secondary Ion Mass Spectrometry. *Int. J. Mass Spectrom. Ion Processes* **1990**, *103*, 45–56.

- (3) Zinner, E. Sputter Depth Profiling of Microelectronic Structures. *J. Electrochem. Soc.* **1983**, *130*, 199C–222C.

- (4) Weibel, D.; Wong, S.; Lockyer, N.; Blenkinsopp, P.; Hill, R.; Vickerman, J. C. A C60 Primary Ion Beam System for Time of Flight Secondary Ion Mass Spectrometry: Its Development and Secondary Ion Yield Characteristics. *Anal. Chem.* **2003**, *75*, 1754–1764.

- (5) Touboul, D.; Halgand, F.; Brunelle, A.; Kersting, R.; Tallarek, E.; Hagenhoff, B.; Lapr v te, O. Tissue Molecular Ion Imaging by Gold Cluster Ion Bombardment. *Anal. Chem.* **2004**, *76*, 1550–1559.

- (6) Touboul, D.; Kollmer, F.; Niehuis, E.; Brunelle, A.; Lapr v te, O. Improvement of Biological Time-of-Flight-Secondary Ion Mass Spectrometry Imaging with a Bismuth Cluster Ion Source. *J. Am. Soc. Mass Spectrom.* **2005**, *16*, 1608–1618.

- (7) Appelhans, A. D.; Delmore, J. E. Comparison of Polyatomic and Atomic Primary Beams for Secondary Ion Mass Spectrometry of Organics. *Anal. Chem.* **1989**, *61*, 1087–1093.

- (8) Gillen, G.; Roberson, S. Preliminary Evaluation of an SF₅⁺ Polyatomic Primary Ion Beam for Analysis of Organic Thin Films by Secondary Ion Mass Spectrometry. *Rapid Commun. Mass Spectrom.* **1998**, *12*, 1303–1312.

- (9) K tter, F.; Benninghoven, A. Secondary Ion Emission from Polymer Surfaces under Ar⁺, Xe⁺ and SF₅⁺ Ion Bombardment. *Appl. Surf. Sci.* **1998**, *133*, 47–57.

- (10) Cheng, J.; Winograd, N. Depth Profiling of Peptide Films with ToF-Sims and a C60 Probe. *Anal. Chem.* **2005**, *77*, 3651–3659.

- (11) Winograd, N. The Magic of Cluster Sims. *Anal. Chem.* **2005**, *77*, 142A–149A.

- (12) Yamada, I.; Matsuo, J.; Toyoda, N.; Kirkpatrick, A. Materials Processing by Gas Cluster Ion Beams. *Mater. Sci. Eng.: R: Rep.* **2001**, *34*, 231–295.

- (13) Rabbani, S.; Barber, A. M.; Fletcher, J. S.; Lockyer, N. P.; Vickerman, J. C. ToF-Sims with Argon Gas Cluster Ion Beams: A Comparison with C60⁺. *Anal. Chem.* **2011**, *83*, 3793–3800.

- (14) Ninomiya, S.; Ichiki, K.; Yamada, H.; Nakata, Y.; Seki, T.; Aoki, T.; Matsuo, J. Precise and Fast Secondary Ion Mass Spectrometry Depth Profiling of Polymer Materials with Large Ar Cluster Ion Beams. *Rapid Commun. Mass Spectrom.* **2009**, *23*, 1601–1606.

- (15) Angerer, T. B.; Blenkinsopp, P.; Fletcher, J. S. High Energy Gas Cluster Ions for Organic and Biological Analysis by Time-of-Flight Secondary Ion Mass Spectrometry. *Int. J. Mass Spectrom.* **2015**, *377*, 591–598.

- (16) Lee, J. L. S.; Ninomiya, S.; Matsuo, J.; Gilmore, I. S.; Seah, M. P.; Shard, A. G. Organic Depth Profiling of a Nanostructured Delta Layer Reference Material Using Large Argon Cluster Ions. *Anal. Chem.* **2009**, *82*, 98–105.

- (17) Sheraz n e Rabbani, S.; Barber, A.; Fletcher, J. S.; Lockyer, N. P.; Vickerman, J. C. Enhancing Secondary Ion Yields in Time of Flight-Secondary Ion Mass Spectrometry Using Water Cluster Primary Beams. *Anal. Chem.* **2013**, *85*, 5654–5658.

- (18) Sheraz n e Rabbani, S.; Razo, I. B.; Kohn, T.; Lockyer, N. P.; Vickerman, J. C. Enhancing Ion Yields in Time-of-Flight-Secondary Ion Mass Spectrometry: A Comparative Study of Argon and Water Cluster Primary Beams. *Anal. Chem.* **2015**, *87*, 2367–2374.

- (19) Wucher, A.; Tian, H.; Winograd, N. A Mixed Cluster Ion Beam to Enhance the Ionization Efficiency in Molecular Secondary Ion Mass Spectrometry. *Rapid Commun. Mass Spectrom.* **2014**, *28*, 396–400.

- (20) Toyoda, N.; Yamada, I. Reduction of Irradiation Damage Using Size-Controlled Nitrogen Gas Cluster Ion Beams. *Nucl. Instr. Methods Phys. Res. Sect. B: Beam Interactions Mater. Atoms* **2012**, *273*, 11–14.

- (21) Takaoka, G. H.; Ryuto, H.; Takeuchi, M. Surface Irradiation and Materials Processing Using Polyatomic Cluster Ion Beams. *J. Mater. Res.* **2012**, *27*, 806–821.

- (22) Ryuto, H.; Ozaki, R.; Mukai, H.; Takaoka, G. H. Interaction between Ethanol Cluster Ion Beam and Silicon Surface. *Vacuum* **2010**, *84*, 1419–1422.

- (23) Paruch, R. J.; Garrison, B. J.; Mlynek, M.; Postawa, Z. On Universality in Sputtering Yields Due to Cluster Bombardment. *J. Phys. Chem. Lett.* **2014**, *5*, 3227–3230.

- (24) Seah, M. P. Universal Equation for Argon Gas Cluster Sputtering Yields. *J. Phys. Chem. C* **2013**, *117*, 12622–12632.
- (25) Seah, M. P.; Havelund, R.; Gilmore, I. S. Universal Equation for Argon Cluster Size-Dependence of Secondary Ion Spectra in Sims of Organic Materials. *J. Phys. Chem. C* **2014**, *118*, 12862–12872.
- (26) Shard, A. G.; et al. Argon Cluster Ion Beams for Organic Depth Profiling: Results from a Vamas Interlaboratory Study. *Anal. Chem.* **2012**, *84*, 7865–7873.
- (27) Lee, J. L. S.; Ninomiya, S.; Matsuo, J.; Gilmore, I. S.; Seah, M. P.; Shard, A. G. Organic Depth Profiling of a Nanostructured Delta Layer Reference Material Using Large Argon Cluster Ions. *Anal. Chem.* **2010**, *82*, 98–105.
- (28) Cheng, J.; Winograd, N. Depth Profiling of Peptide Films with ToF-Sims and a C60 Probe. *Anal. Chem.* **2005**, *77*, 3651–3659.
- (29) Cheng, J.; Wucher, A.; Winograd, N. Molecular Depth Profiling with Cluster Ion Beams. *J. Phys. Chem. B* **2006**, *110*, 8329–8336.
- (30) Wucher, A.; Cheng, J.; Winograd, N. Molecular Depth Profiling Using a C60 Cluster Beam: The Role of Impact Energy. *J. Phys. Chem. C* **2008**, *112*, 16550–16555.
- (31) Fletcher, J. S.; Rabbani, S.; Henderson, A.; Blenkinsopp, P.; Thompson, S. P.; Lockyer, N. P.; Vickerman, J. C. A New Dynamic in Mass Spectral Imaging of Single Biological Cells. *Anal. Chem.* **2008**, *80*, 9058–9064.
- (32) Mao, D.; Wucher, A.; Winograd, N. Molecular Depth Profiling with Cluster Secondary Ion Mass Spectrometry and Wedges. *Anal. Chem.* **2010**, *82*, 57–60.
- (33) Lu, C.; Wucher, A.; Winograd, N. Ionization Effects in Molecular Depth Profiling of Trehalose Films Using Buckminsterfullerene (C60) Cluster Ions. *Surf. Interface Anal.* **2011**, *43*, 99–102.
- (34) Holzweber, M.; Shard, A. G.; Jungnickel, H.; Luch, A.; Unger, W. E. S. Dual Beam Organic Depth Profiling Using Large Argon Cluster Ion Beams. *Surf. Interface Anal.* **2014**, *46*, 936–939.
- (35) Acree, W.; Chickos, J. S. Phase Transition Enthalpy Measurements of Organic and Organometallic Compounds. Sublimation, Vaporization and Fusion Enthalpies from 1880 to 2010. *J. Phys. Chem. Ref. Data* **2010**, *39*, No. 043101.
- (36) Higashiyama, T. Novel Functions and Applications of Trehalose. *Pure Appl. Chem.* **2002**, *74*, 1263.
- (37) Wucher, A. A Simple Erosion Dynamics Model of Molecular Sputter Depth Profiling. *Surf. Interface Anal.* **2008**, *40*, 1545–1551.
- (38) Mao, D.; Lu, C.; Winograd, N.; Wucher, A. Molecular Depth Profiling by Wedged Crater Beveling. *Anal. Chem.* **2011**, *83*, 6410–6417.